Space Nuclear Power Systems - Direct Fusion Drive

Michael A. Paluszek[*]   Stephanie J. Thomas[†]

Eric Hinterman[‡] Yukino Nagai [‡] Lisa Peng [‡] Audrey Walsh [‡]

Princeton Satellite Systems, Plainsboro, NJ, 08536, US

Samuel A. Cohen[§]

Gabriel Gaitan,[¶] Eric Ham [‡]

Princeton Plasma Physics Laboratory, Princeton, NJ, 08543, US

The Direct Fusion Drive (DFD) is a small fusion reactor that has the potential to revolutionize space power and propulsion. Direct Fusion Drive is based on the Princeton Field-Reversed Configuration reactor concept from Princeton Plasma Physics Laboratory. We have been using our NASA funding to explore the balance of plant for this unique engine, which can provide both megawatts of electric power and multi-Newtons of thrust in a single integrated device.

The engine has an array of field shaping coils with two smaller but higher field mirror coils. Coolant lines running along the fusion chambeer collect thermal energy from the neutrons, bremsstrahlung radiation, and synchrotron radiation for producing electricity. A ~1 kW neutral beam injects the fusion fuel into the center of the engine, while propellant enters from the ionizing gas box on the end opposite the nozzle.

This paper will present the latest work on sizing a Brayton engine for DFD and compare a typical Xenon-Helium coolant engine to a supercritical carbon dioxide engine. The coolant lines for the thermal engine will need to run through the engine's shielding, which must absorb sufficient heat and neutrons to protect the superconductors and their cooling systems. This is a complex and interesting engineering problem, which we are addressing in parallel with development of the core fusion physics.

The paper will begin with a short summary of the DFD technology. We will then present the latest work on sizing the Brayton engine, and comparing the Xenon-Helium option to supercritical carbon dioxide. We will then briefly review the preliminary design for the space radiators and provide a mass breakdown showing the estimated specific power achievable. Results on the RF generation system and on the power generators are also presented.

I.   Introduction

Ambitious new missions, both robotic and with human crews, would benefit from new propulsion systems and power systems. Propulsion systems with higher exhaust velocities at high thrust would reduce trip times. Higher power would allow for high data transmission rates and new types of experiments. Current deep space robotic missions are limited to power in the hundreds of watts. This presents a challenge to the payload designers and provides a constraint on the rate of data delivery that is, all other things being equal, proportional to power. The mission durations are set by the low specific impulse of chemical rocket engines. Electric propulsion systems can improve this but are limited by the combined specific power of the engine and power plants. Human missions to Mars or the Moon are also limited by propulsion and power. Human bases on the moon and Mars will require considerable power. Solar is problematic on the moon as storage

---

[*]President
[†]Vice President, AIAA Senior Member.
[‡]Intern
[§]Professor, Princeton University, Princeton, NJ
[¶]Intern

American Institute of Aeronautics and Astronautics

is needed for lunar nights. Mars bases would likely require nuclear power plants but the launching of large amounts of fissionable material is an issue. The specific impulse of chemical engines leads to long coast times and aerodynamic braking at the destinations that complicates mission planning.

Figure 1 shows an artist's rendering of a DFD rocket engine that has the potential to solve these problems. It produces both power and propulsion in a single unit. It can also be configured just as a power plant for orbital or surface power. The simple geometry leads to a relatively high specific power, enabling shorter mission durations such as a four year mission to reach Pluto and go into orbit. Numerous papers have been written on this technology[1-7] exploring many different missions.
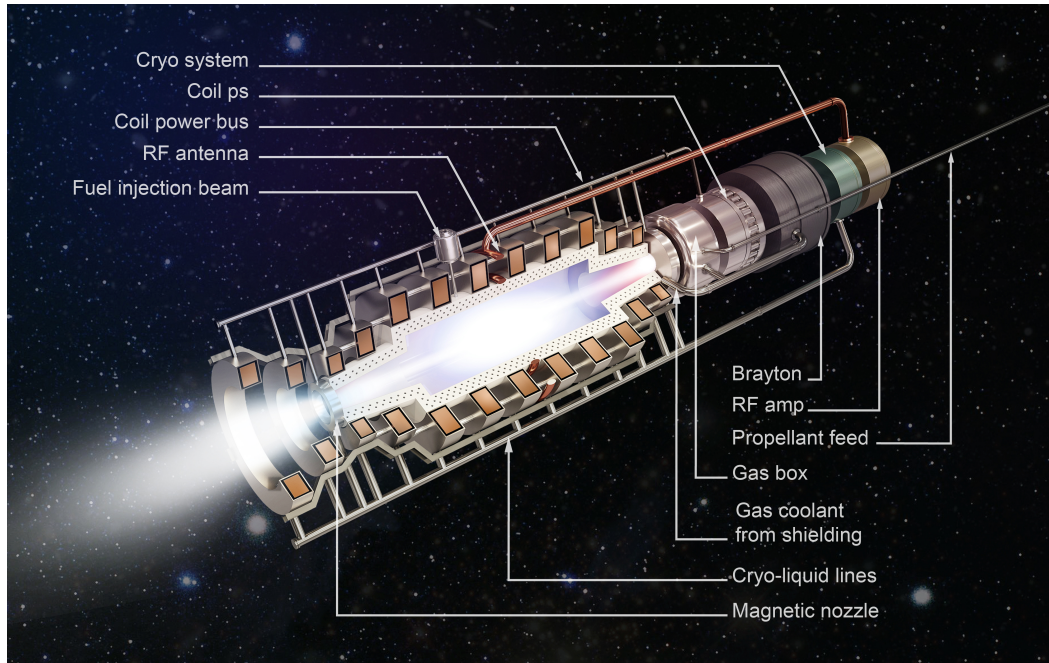
Figure 1. Artist's Rendering of the Direct Fusion Drive, based on the Princeton Field-Reversed Configuration fusion reactor

This paper will explore the energy recycling of the engine. Recycled energy is needed to drive the fusion reactions. Energy that is leftover from that process can power other systems on the spacecraft.

II.   Direct Fusion Drive

The Direct Fusion Drive concept is an extension of ongoing fusion research at Princeton Plasma Physics Laboratory dating to 2002.[8-11] The Princeton Field-Reversed Configuration machine (PFRC) employs a unique radio frequency (RF) plasma heating method. Odd-parity heating was first theorized in 2000[12] and demonstrated in the 4 cm radius PFRC-1 experiment in 2006.[13] Experiments are ongoing with the second-generation machine, PFRC-2, which has a coil inner radius of 8 cm (Figure 2). Studies of electron heating in PFRC-2 have surpassed theoretical predictions, recently reaching 500 eV with pulse lengths of 300 ms. Experiments to measure ion heating with input power up to 200 kW are ongoing. When scaled up to achieve fusion parameters, PFRC would result in a 4-8 m long, 1.5 m diameter reactor producing 1 to 10 MW. This reactor would be uniquely small and clean among all fusion reactor concepts, producing remarkably low levels of damaging neutrons.

The plasma heating method uses a unique configuration of the radio frequency antenna. Attempts have been made to heat FRC plasmas with RF before, but always with picture-frame antenna that resulted in a near-FRC plasma but with open field lines. We call this even-parity heating due to the symmetry of the induced magnetic field. Open field lines give the plasma an opportunity to escape and reduce confinement time. In contrast, each of the four PFRC antennae sections are two joined rectangles. Two pairs operate 90 degrees out of phase on adjacent sides of the plasma. An antenna (wrapped in orange Kapton tape) is clearly visible on the side of PFRC-2 in Figure 2. This results in so-called odd-parity heating - the magnetic field on one side of each figure-8 is in the opposite direction as the other side - and closed field lines in the

American Institute of Aeronautics and Astronautics
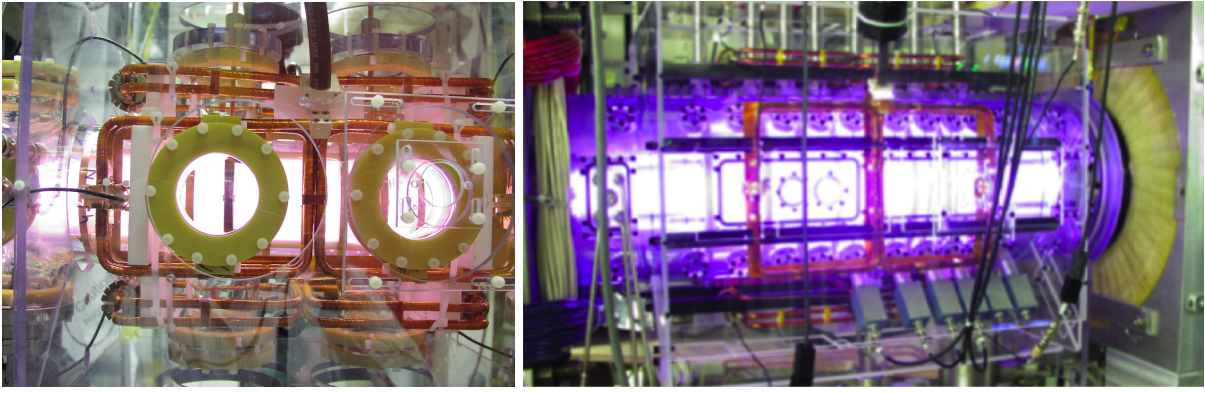
Figure 2. PFRC-1 and PFRC-2 Experiments. The RF antennae are visible wrapped in orange Kapton tape.

generated FRC. Closed field lines keep the plasma trapped as it is heated. The oscillation of the currents in the RF antenna result in a rotating magnetic field, RMF, with about 0.1-1% of the strength of the axial magnetic field.

Reduction in neutrons is achieved through multiple means. First and foremost, our choice of Helium-3 (^{3}He) and deuterium (D) fuels results in an aneutronic primary reaction. However, there are still D-D side reactions, the proportion of which is governed by the fusion cross-section at the relevant ion temperature. The D-D side reactions are divided equally into two, a D-D reaction producing a 2.45 MeV neutron and a D-D reaction producing tritium (T). This tritium can then fuse with deuterium to produce a high energy 14.7 MeV neutron.

$$D + {}^3He \quad \rightarrow \quad {}^4He \ (3.6 \ \text{MeV}) + p \ (14.7 \ \text{MeV}) \tag{1}$$

$$D + D \quad \rightarrow \quad T \ (1.01 \ \text{MeV}) + H \ (3.02 \ \text{MeV}) \tag{2}$$

$$D + D \quad \rightarrow \quad {}^3He \ (0.82 \ \text{MeV}) + n \ (2.45 \ \text{MeV}) \tag{3}$$
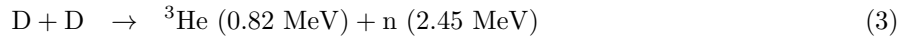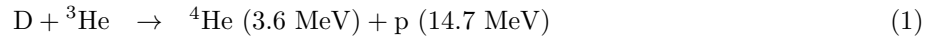
The PFRC is specifically designed to reduce the number of neutrons produced from these side reactions. One, the small size of the reactor results in a favorable ratio of surface area to plasma volume, reducing the wall load compared to larger machines. Two, we adjust the operating fuel ratio of ^{3}He:D to 3:1, sacrificing some power density for lower neutron production. Three, the reactor is designed to rapidly eliminate the tritium produced by the D-D side reactions, preventing any D-T reactions from occurring. This means that the only neutrons produced are those with energy of 2.45 MeV. A fourth reduction in neutrons may occur due to preferential heating of the ^{3}He over the D by the rotating magnetic fields; at the correct frequency, we estimate that the ^{3}He may reach a temperature of 140 keV while the D is only at 70 keV. This would result in another 5- to 10-fold reduction in neutrons. The final result of these design features is that less than 1% of the fusion power is in 2.45 MeV neutrons, the power in 14.7 MeV neutrons is effectively zero and the wall load, E/m^2 is 1/1000 or less that in a D-T tokamak.

The tritium is eliminated due to its interaction with the cool scrape-off-layer (SOL) surrounding the fusion region. The size of the reactor is such that the plasma physics s factor, which scales with the ratio of the ion gyro-radius to the scrape-off-layer radius, is low - about 2.3. This forces the tritons to pass through the SOL repeatedly. When the tritons pass through the cool SOL plasma, electron drag causes energy to be transferred from the tritons to the SOL electrons.[14] The triton is quickly captured by the SOL field lines and flows out the open end of the reactor. The burn-up time for energetic tritons to fuse is about 20 seconds, while the time in which it will cool and be trapped in the SOL is less than 0.01 s.[3] The same process occurs for the other fusion ash products, which are all effectively exhausted.

Parameter	DFD
Fuel	D-^{3}He
r_s	0.3 m
Elongation, κ	5
B_{axial}	4.3 T
B_{nozzle}	20 T
B_{RMF}/B_{axial}	0.003
β	0.84
^{3}He:D	2
n_e	3 $\times 10^{20}$ m^{-3}
T_e	30 keV
T_i	100 keV
P_f	0.99 MW
S*/κ	2.8
γ_{LH}	0.02
s_{T+}	2.3
s_{fuel}	10

Table 1. Parameters for a 1-MW engine

American Institute of Aeronautics and Astronautics

The subsystems are shown in Figure 3. This paper will focus on the heat recycling subsystems. These are the components in the lower right hand side of the diagram.
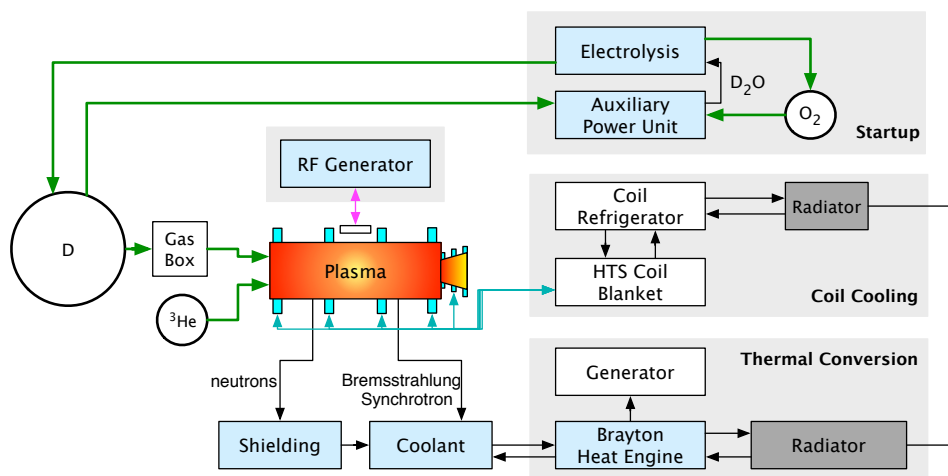
Figure 3. DFD subsystems. The major subsystems are indicated with gray boxes.

III. Heat Recovery System Analysis

The heat recovery system must recycle waste heat and convert it to power to drive the RMF_o which heats the reactants to fusion temperature. The complete power cycle is shown in Figure 4.
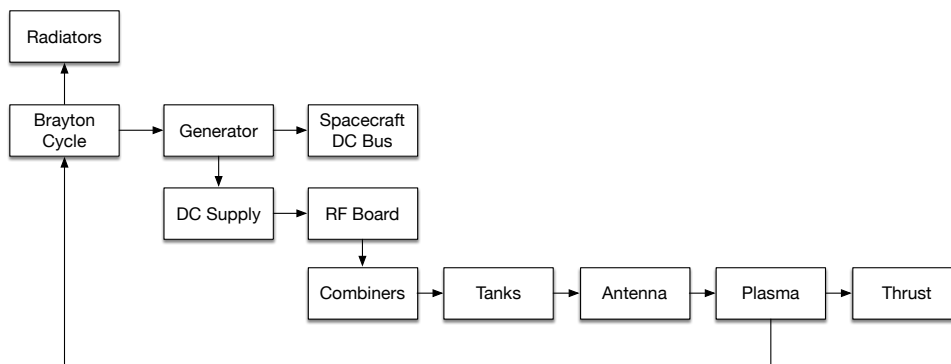
Figure 4. DFD power cycle. The arrows show the flow of energy in the system.

A Xenon/Helium working fluid Brayton cycle and a supercritical CO_2 cycle were analyzed. This section will first discuss the waste heat problem. It will then present analyses of the two systems. It will then discuss turbomachinery and radiators for the low pressure Xenon/Helium system.

III.A. Waste Heat

Waste heat comes from x-rays from bremsstrahlung, synchrotron radiation and wall heating. X-rays are absorbed as they pass through materials according to the exponential law[15]

$$\frac{I}{I_0} = e^{-\frac{\mu}{\rho}x} \tag{4}$$

where I_0 is the incident intensity, I is the (reduced) intensity after traveling a distance x through the material, ρ is the material density, μ is the attenuation coefficient, and $\frac{\mu}{\rho}$ is the *mass* attenuation coefficient (sometimes also referred to as the photoelectric absorption (coefficient) due to photo-electron energy losses being the principal cause). Tungsten is the best x-ray attenuator at all but extremely low energies but stainless steel, titanium and the coolant all absorb significant x-rays as well.

American Institute of Aeronautics and Astronautics

The wavelength dependence is cubic with discontinuities at wavelengths corresponding to specific electronic transitions within the absorbing atoms. X-Ray absorption happens in both the coolant gas and the metal absorption material. For a helium/xenon mixture the mass attenuation coefficient is

$$\frac{\mu}{\rho} = 0.7 \left(\frac{\mu}{\rho}\right)_{Xe} + 0.3 \left(\frac{\mu}{\rho}\right)_{He} \tag{5}$$

Figure 5 shows the attenuation coefficients for titanium, beryllium, iron, and tungsten. [a]
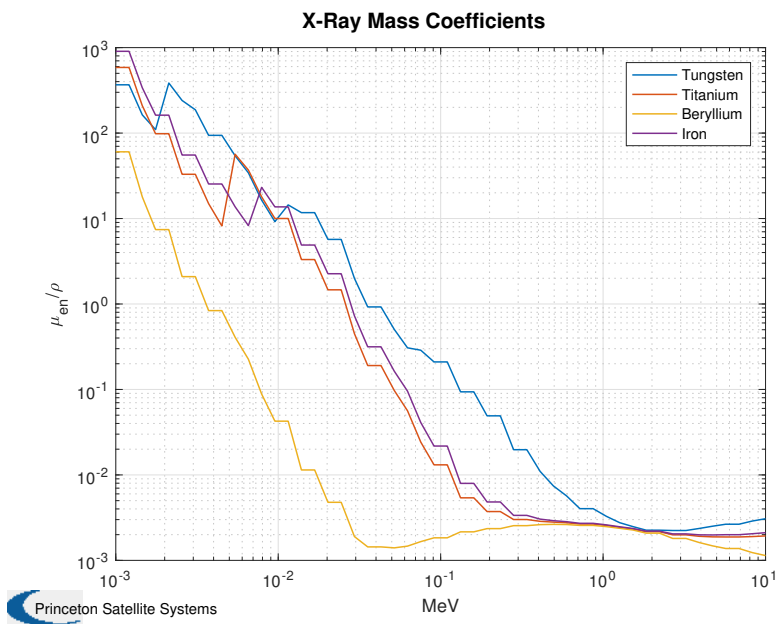
Figure 5. X-ray coefficients. Sample materials are shown.

Figure 7 shows the spectrum of emission for 30 keV electrons. The frequency cutoff can be calculated from the temperature,

$$\nu_{cutoff} > kT/h$$

so for 30 keV electrons, the frequency cutoff is $7.25e^{18}$ Hz. (1 eV is 11604.5 K). This is a wavelength of 4.1376e-11 m, or 0.04 nm. X-rays are in the range of 0.01 to 10 nm, and shorter wavelengths are classified as gamma rays, so these are very energetic x-rays. The 30 keV temperature is for a Maxwellian distribution, so there will be a population of higher energy electrons, with 45 keV as the mean. Figure 6 shows the attenuation in a 1 mm layer of titanium.

Synchrotron radiation is also a source of waste heat. Figure 8 shows two models, the NRL formulary and Bingren's[16]

III.B. Supercritical CO$_2$ Brayton Cycle

The supercritical CO$_2$ cycle is shown in Figure 9. The cycle operates with CO$_2$ at the supercritical point. CO$_2$ is kept above the supercritical point where it has properties of both a gas and a liquid. It allows for very compact machinery. The high pressures, greater than 7 MPa, result in very compact, albeit heavy, machinery. The recuperators are CO$_2$ to CO$_2$ heat exchangers.

The results from a thermodynamic model of the system are shown in Figure 10. The results show that the efficiency goes down as the pressure ratio goes up, which is consistent with expectation. The results of this analysis suggests that a low pressure of 7.5 MPa is not the ideal low pressure, because the highest efficiency was achieved when the low pressure was at around 16 MPa and the high pressure was at 25 MPa. As more fluid is sent to the radiator, more heat is lost to the environment, and thus the efficiency decreases. However, too low of a percentage results in a non-physical recuperator that requires the hot temperature to be too low.

---

[a]http://www.nist.gov/pml/data/xraycoef/index.cfm
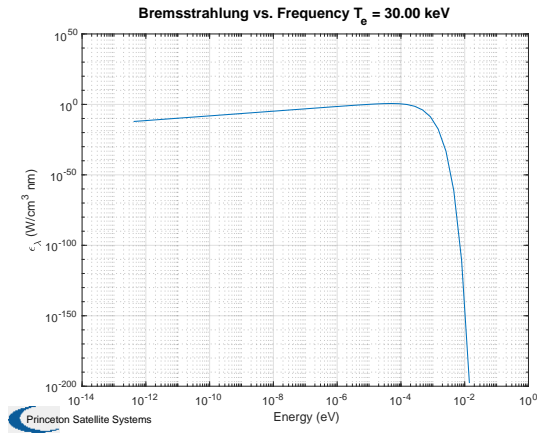
Figure 6. X-ray attenuation in 0.1 mm of titanium. A thin film is sufficient to absorb all x-rays.
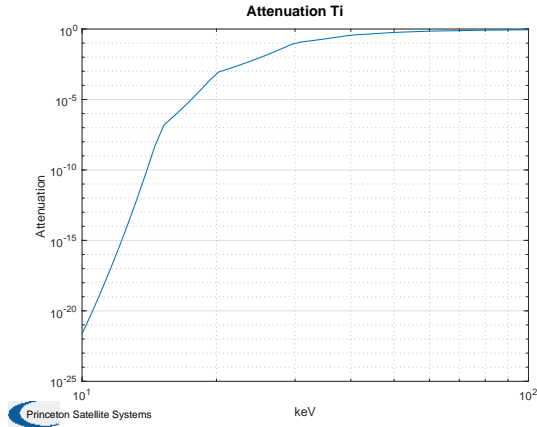
Figure 7. Bremsstrahlung spectrum for 30 keV electrons. The spectrum shows a sharp cutoff.
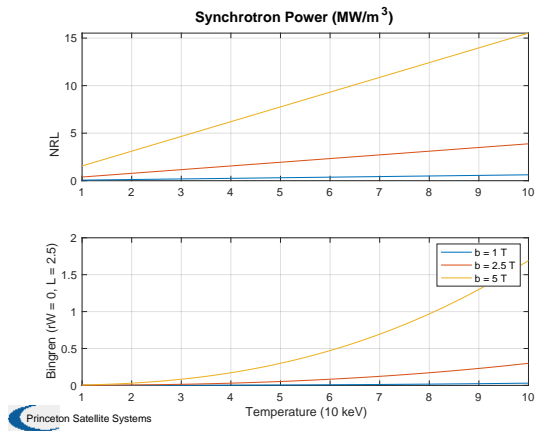
Figure 8. Synchrotron. Bingren's and the NRL model are shown.

American Institute of Aeronautics and Astronautics
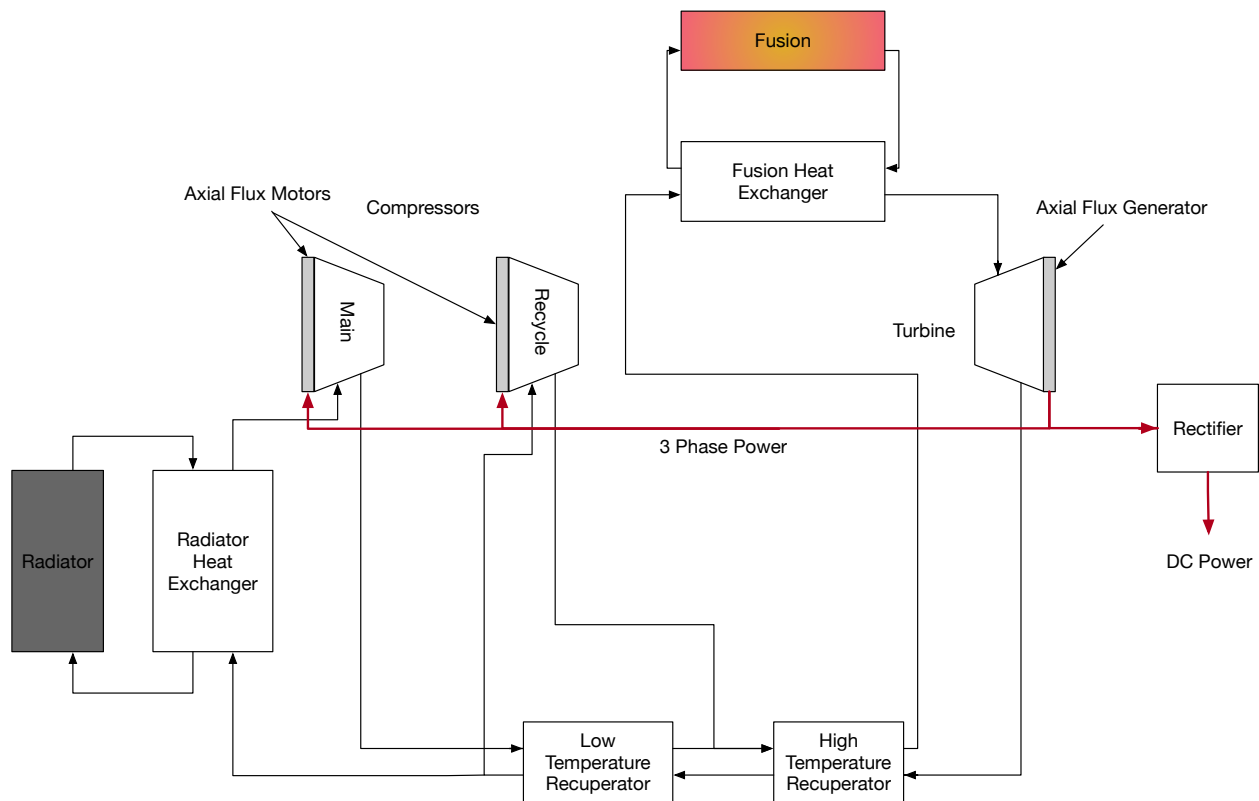
Figure 9. Supercritical CO_2 cycle. Very high efficiencies are possible.
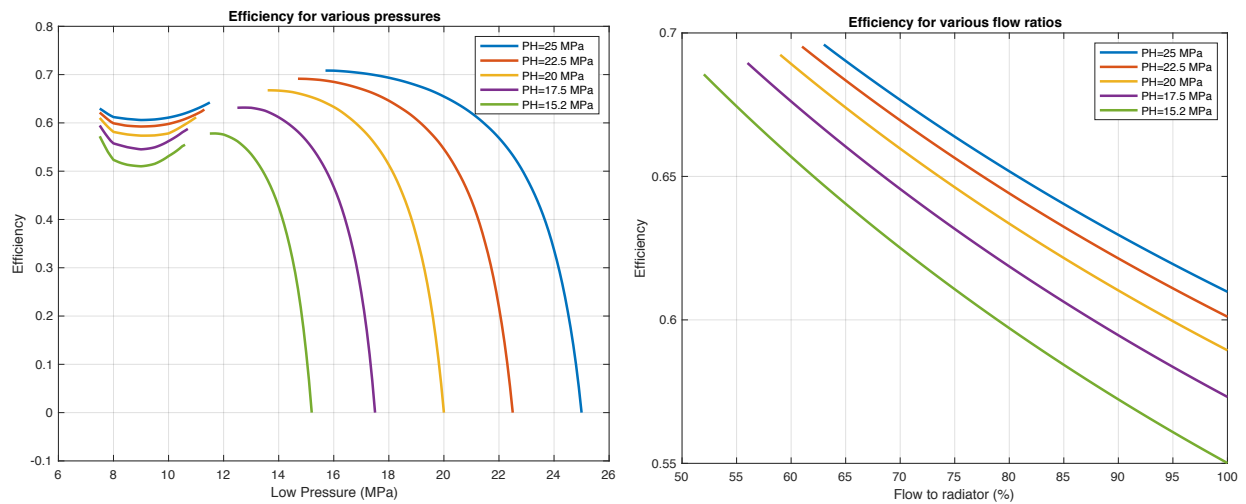
Figure 10. Efficiency of the recompression cycle. A flow rate of 0.9 and various pressures (left) and the efficiency at various flow rates (right).

American Institute of Aeronautics and Astronautics

The efficiency of the recompression cycle is greater than a simple cycle. In a fusion rocket, the specific power matters more than the efficiency. The power output gained from the extra 10-15% efficiency must sufficiently outweigh the mass increase from having additional components onboard. The results presented above provide promising results for the possibility of a supercritical CO_2 Brayton power cycle for DFD.

III.C. Low Pressure Brayton Cycle

Several working fluid options have been considered for Brayton Cycles with similar applications to this proposal. Monatomic working fluids of interest include Helium (He), Argon (Ar), and Xenon (Xe). All are noble gases and are thus stable and non-reactive. Diatomic working fluids include Nitrogen (N_2) and Hydrogen (H_2). Carbon Dioxide (CO_2) has been considered as a polyatomic working fluid. Finally, gas mixtures are often considered, including He-Ar and He-Xe. These working fluids and their properties are summarized in Table 2 and Table 3.

Fluid	Symbol	M g/mole	C_p J/kg-K	C_v J/kg-K	κ mW/m-K
Helium	He	4.0	5193	3157	360
Argon	Ar	40.0	520	312	42
Xenon	Xe	131.3	160	97	16
Nitrogen	N_2	28.0	1170	741	68
Hydrogen	H_2	2.0	14980	10700	430
Carbon Dioxide	CO_2	44.0	1234	1070	74
Helium/Xenon	He-Xe	42.2	494	300	39
Helium/Argon	He-Ar	14.8	1405	911	265

Table 2. Properties of working fluids taken at 1000 K. M is the molar mass, C_p is the specific heat at constant pressure, C_v is the specific heat at constant volume, and κ is the thermal conductivity.

It is important to note that certain properties of the working fluids vary with temperature. These include dynamic viscosity (μ), thermal conductivity (κ), and thermal capacity (C_p and C_v). For example, thermal capacity varies with temperature for all working fluids that are not comprised of noble gases. An example is given in Figure 11, which shows the thermal capacity variation of N_2 and CO_2 with temperature. Helium/Xenon provides the best option as its combination of fluid properties and thermal properties result in high efficiencies and low masses. As the fluid properties are similar to air conventional turbomachinery can be used.

Fluid	C_p (J/kg-K)	κ W/m-K	μ 10^6Pa-s	γ	M kg/mole
Ar	523	0.016	21.0	1.66	0.04
He	5190	0.142	19.0	1.66	0.004
N_2	1040	0.024	16.6	1.40	0.028
CO_2	849	0.015	9	1.28	0.044

Table 3. Properties of working fluids taken at 288 K. C_p is the thermal capacity, κ is the thermal conductivity, μ is the dynamic viscosity, γ is the ratio of specific heats and M is the molar mass. The values are taken at 288 deg-K.

The low pressure cycle is shown in Figure 12. Note that the black lines indicate a physical axle connection between two pieces of turbomachinery, while the colored lines indicate the working fluid path. The shaft may be replaced by an electrical transmission that would also eliminate the need for two turbines. The working fluid first enters Compressor 1. The compressor is driven by Turbine 1, though it will need power at the start of the cycle from elsewhere. This will come from the D_2/O_2 combustion that also powers the start-up of the Heater. The fluid's pressure and temperature increase as it passes through Compressor 1. In order to maximize efficiency of subsequent compressors, the fluid will be cooled before entering each one. After exiting the last compressor, it may be passed through a Recuperator in order to be pre-heated. This depends on the mission's operating parameters and the power dissipation of the Heater. After the Recuperator, the working fluid will pass into cooling coils that loop around the nuclear reactor. At this point, the working fluid will be heated to very high temperatures - around 1500 K - through radiation absorption. This hot fluid will then be passed through a series of turbines in order to generate power. The compressors will be directly driven by turbines, and the turbines that remain at the end of the series will be used to drive an electricity-producing generator. After passing out of the turbines, the gas will have cooled but will still be relatively hot. It also will have dropped to roughly the same pressure as the inlet stream to Compressor 1. The gas may pass through a recuperator to further cool it before being passed into the pre-cooler heat exchanger to bring it down to its original temperature.

American Institute of Aeronautics and Astronautics
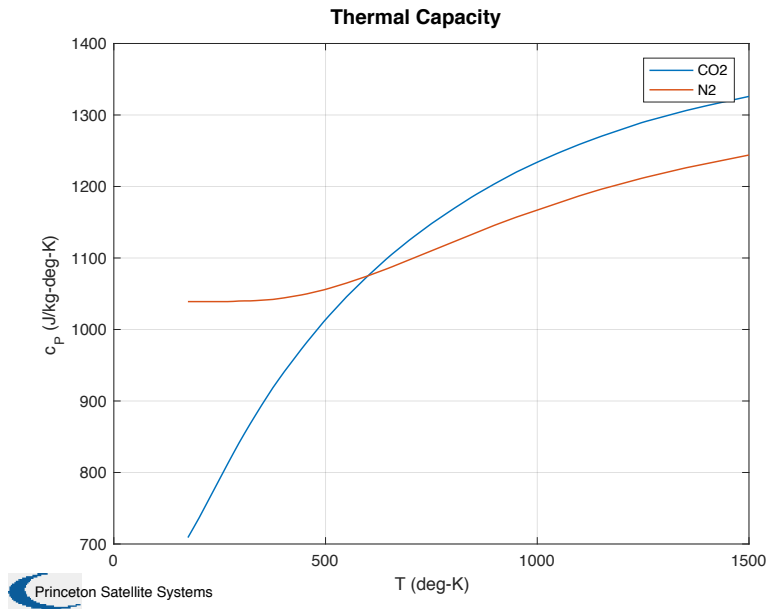
Figure 11. The thermal capacity for N_2 and CO_2. The figure shows the variations with temperature.
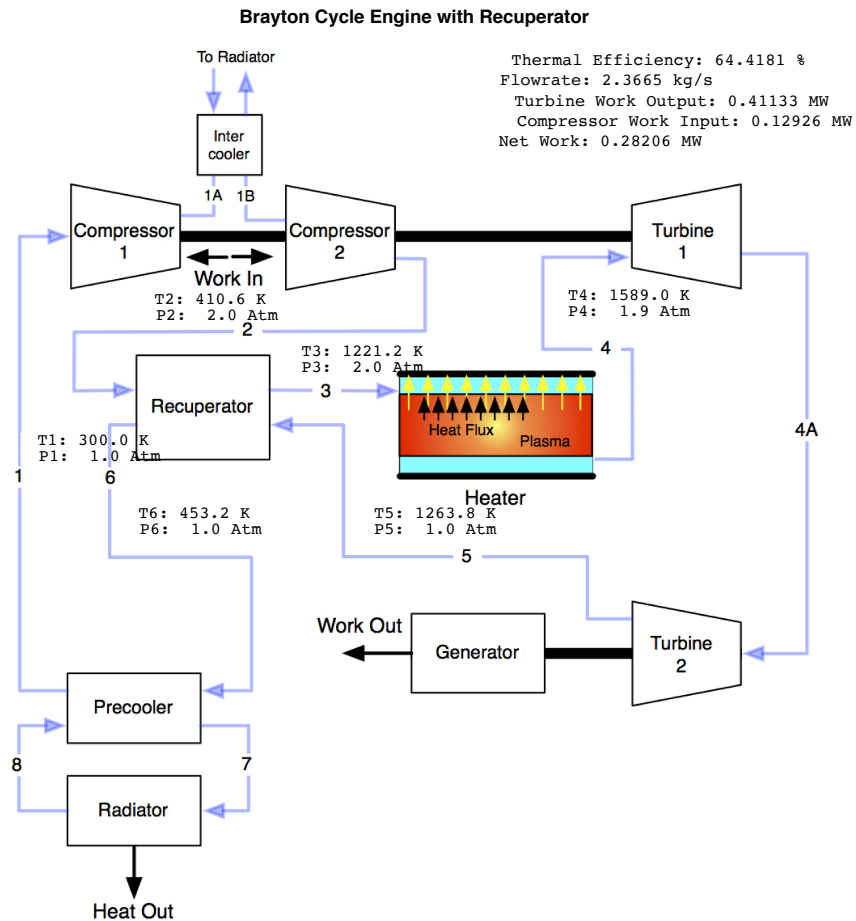
Figure 12. Low pressure Brayton cycle. The cycle has a recuperator and dual compressors and turbines.

American Institute of Aeronautics and Astronautics

III.D.   Heat Exchanger

III.D.1.   Introduction

The heat transfer geometry is shown in Figure 13. A cross-sectional view is shown in Figure 14. This is the typical design for combustors or rocket engine nozzles.The gas in the heat exchanger ranges from 300 deg-K at the inlet to 1589 deg-K at the outlet. The fusion chamber and superconducting coils are both wrapped in MLI. The following section discuss the geometry, the multi-layer insulation (MLI) and the convection heat flow analysis.
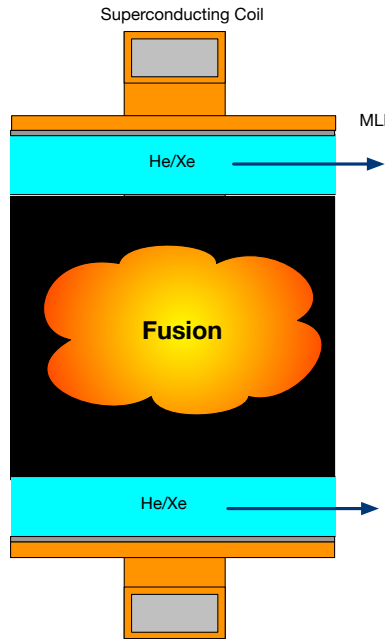
Figure 13. Heat transfer geometry. The figure shows the reactor and superconducting coils. The coolant runs axially along the outside of the pressure vessel. This does not show shielding.
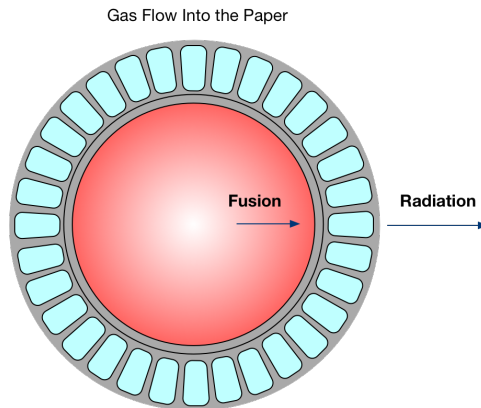
Figure 14. Heat exchanger cross-section. The web thicknesses are conceptual.

In the heat exchanger the pressure is 2 Atm. The heat exchanger is an annulus around the fusion reactor. The hoop stress is

$$\sigma_\theta = \frac{Pr}{t} \tag{6}$$

where P is the pressure, r is the radius and t is the wall thickness. The minimum tensile strength of SiC is 240 MPa.[17] Thus the wall thickness for a 0.3 m radius reactor is 0.5 mm for a typical ceramic heat exchanger. The energy balance for the shell is

$$\alpha_s q_s = \sigma \epsilon_s T_s^4 + k(T_s - T_i) \tag{7}$$

American Institute of Aeronautics and Astronautics

$$\alpha_s q_s - \sigma \epsilon_s T_s^4 \quad = \quad \sigma \epsilon_i T_i^4 \tag{8}$$

where α is the absorption, ϵ is the emittance, σ is the Stefan-Boltzmann constant equal to 5.67×10^{-8} Wm^{-2}K^{-4}. The emittance and absorption need to be computed for the band of wavelengths of the light. The very outer shield for the engine will be illuminated by the Sun but the inner walls will see radiation in the infrared bands.

III.D.2.   Multi-layer Insulation (MLI)

The MLI heat flux model is.[18]

$$q = \frac{C_s \bar{N}^\gamma (T_h + T_c)(T_h - T_c)}{N + 1} + \frac{C_r \epsilon_{TR}}{N} \left(T_h^{4.67} - T_c^{4.67} \right) \tag{9}$$

where $\bar{N}$ is the MLI layer density. The first term is for conduction through the spacers which is function of the MLI density and mean temperature. The second term is the radiation heat transfer. ϵ_{TR} is the effective emissivity. This can be put in the form of conductive heat transfer to find an equivalent conductivity k

$$q = k \left(\frac{T_h - T_c}{\delta} \right) \tag{10}$$

and the MLI layer density is

$$\bar{N} = \frac{N}{\delta} \tag{11}$$

where δ is the MLI layer thickness. Assume $N + 1 = N$ for large N. We then get

$$k = a\bar{N}^{\gamma-1} + \frac{b}{\bar{N}} \tag{12}$$

where

$$a \quad = \quad C_s(T_h + T_c) \tag{13}$$

$$b \quad = \quad C_r \epsilon_{TR} \left(\frac{T_h^{4.67} - T_c^{4.67}}{T_h - T_c} \right) \tag{14}$$

We maximize k when

$$\bar{N}^\gamma = \frac{b}{(\gamma - 1)a} \tag{15}$$

Table 4 gives coefficients for blankets tested by Lockheed.

Type	γ	C_s	C_r	ϵ_{TR}
Perforated, Double-Aluminized Mylar/Preconditioned Silk Net	2.84	2.98 $\times 10^{-8}$	5.86 $\times 10^{-10}$	0.043
Preconditioned silk net spacer system	2.56	8.95 $\times 10^{-8}$	5.39 $\times 10^{-10}$	0.031
As received silk net spacer system	3.56	2.11 $\times 10^{-9}$	5.39 $\times 10^{-10}$	0.031

Table 4.   MLI types.

The heat flux from the outer wall is entirely radiative and is

$$\dot{q}_4 = \sigma \epsilon A T_{s_4}^4 \tag{16}$$

If the conduction from the fluid to the outer wall is k then we get the equation

$$\frac{dT_b}{dx} = \frac{\dot{q}_1 - kc(T_b - T_{s_4})}{\dot{m} C_p} \tag{17}$$

where $T_b(0) = T_1$ and

$$\frac{1}{k} = \frac{1}{h} + \frac{1}{k_w} + \frac{1}{k_{\mathrm{MLI}}} \tag{18}$$

American Institute of Aeronautics and Astronautics

The loss is radiative so we can solve for T_{s_4}

$$\sigma \epsilon T_{s_4}^4 = k(T_b - T_{s_4}) \tag{19}$$

where c is the circumference. We find T_{s_4} as a function of T_b by solving the quartic

$$\sigma \epsilon T_{s_4}^4 + kT_{s_4} - kT_b = 0 \tag{20}$$

The quartic will have one complex pair, a negative root and a positive root. The positive root is the temperature.

III.D.3. Convection Heat Transfer

The convection heat transfer coefficient is

$$h = \frac{\text{Nu}\kappa}{D} \tag{21}$$

where Nu is the Nusselt number, κ the thermal conductivity and D is the diameter of the channel. The Nusselt number for turbulent flow is

$$\text{Nu} = \frac{f}{2} \frac{\text{RePr}}{1.07 + 12.7\sqrt{\frac{f}{2}}(\text{Pr}^{\frac{2}{3}} - 1)} \tag{22}$$

Pr is the Prandtl number and is

$$\text{Pr} = \frac{\mu C_p}{\kappa} \tag{23}$$

where C_p is the heat capacity. f is the friction factor and is found from

$$\sqrt{\frac{2}{f}} = 2.46 \log\left(\text{Re}\sqrt{\frac{f}{2}}\right) - 0.292 \tag{24}$$

where the Reynold's number is

$$\text{Re} = \frac{UD}{\nu} \tag{25}$$

where U is the velocity, D the channel diameter and ν is the kinematic viscosity which is

$$\nu = \frac{\mu}{\rho} \tag{26}$$

The kinematic viscosity drops when the density increases thus increasing the Reynold's number. Higher Reynold's numbers lead to turbulent flow which enhances heat transfer. The density is related to the pressure through the ideal gas law

$$\rho = \frac{P}{RT} \tag{27}$$

where R is the gas constant for the particular gas, P is the pressure and T the temperature.

III.D.4. Heat Exchanger Results

The results for a 2.27 cm blanket are shown in Figure 15. The heat flux is an order of magnitude less than the solar flux of 1367 W/m^2.

The best coatings for the outer shell are white organic paints with $\epsilon_s = 0.9$ and $\alpha_s = 0.3$.[19] Varying ϵ_i changes the heat flux from the inner wall as shown in Figure 16. The MLI blanket on the inner wall is 100 layers thick.

The total heat transfer is the sum of the heat emitted by the outer shell and that emitted by the fusion reactor. The outer shell produces 0.07 W/m^2. The peak radiation flux from the fusion chamber is 170 W/m^2 at the hot end of the reactor. Using the same 200 layer blanket we get the results in Table 5. Adjusting the number of layers of MLI in the fusion blanket can reduce the temperatures.
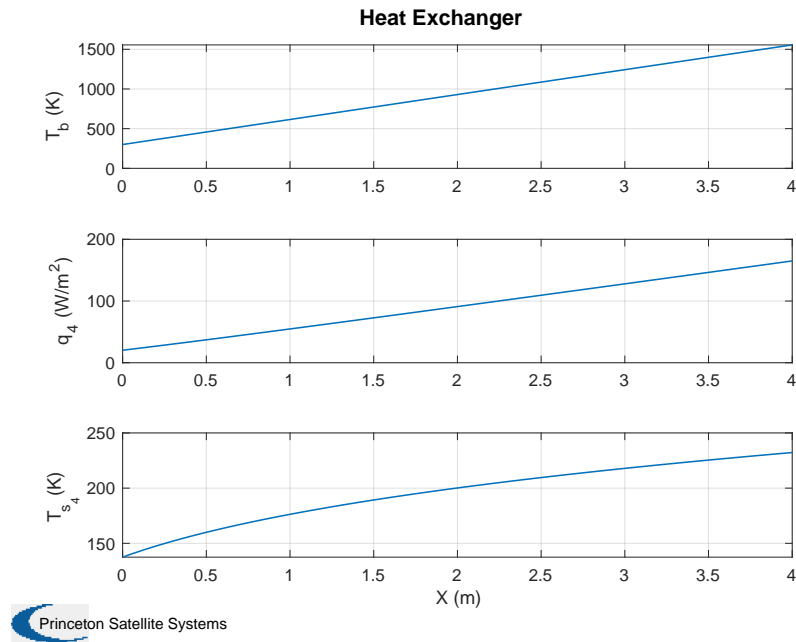
Figure 15. Heat transfer with MLI blanket. The number 4 refers to the outer MLI blanket face.
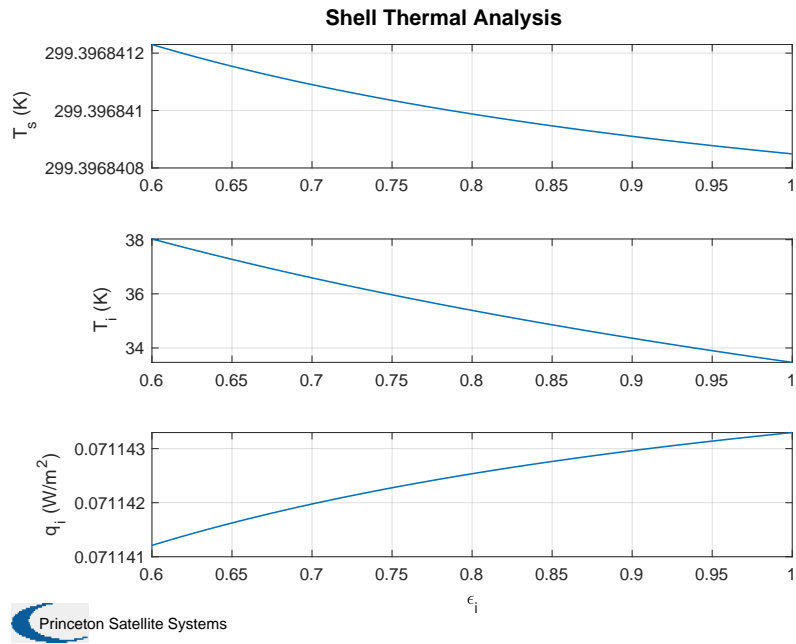
Figure 16. Shell thermal analysis. Varying ϵ_i has little effect. 0.6 to 1.0 is a range for radiator materials.

American Institute of Aeronautics and Astronautics

III.E.   Turbomachinery

The Xenon/Helium cycle uses turbomachinery that is similar to that used in gas turbines that use air as the working fluid. The supercritical CO_2 cycle can use much more compact machinery due the the high pressures. In this analysis, both designs limit the turbine inlet temperature to 1589 deg-K, the temperature limits of GE ceramic turbine blades.

Parameter	Value	Units
Outer shell temperature	177.80	deg-K
Inner shell temperature	27.24	deg-K
Inner shell flux	6.24×10^{-3}	W/m^2
MLI conductance	4.14×10^{-5}	W/m^2

Table 5. Coil heat transfer results.

The remainder of this section focuses on the low pressure cycle. An axial-flow turbine and an axial-flow compressor were designed using mean-line analysis. The Zweiffel Constant and the Diffusion Factor are used to determine the blade geometry. Compressor and turbine blade geometry are shown in Figure 17.
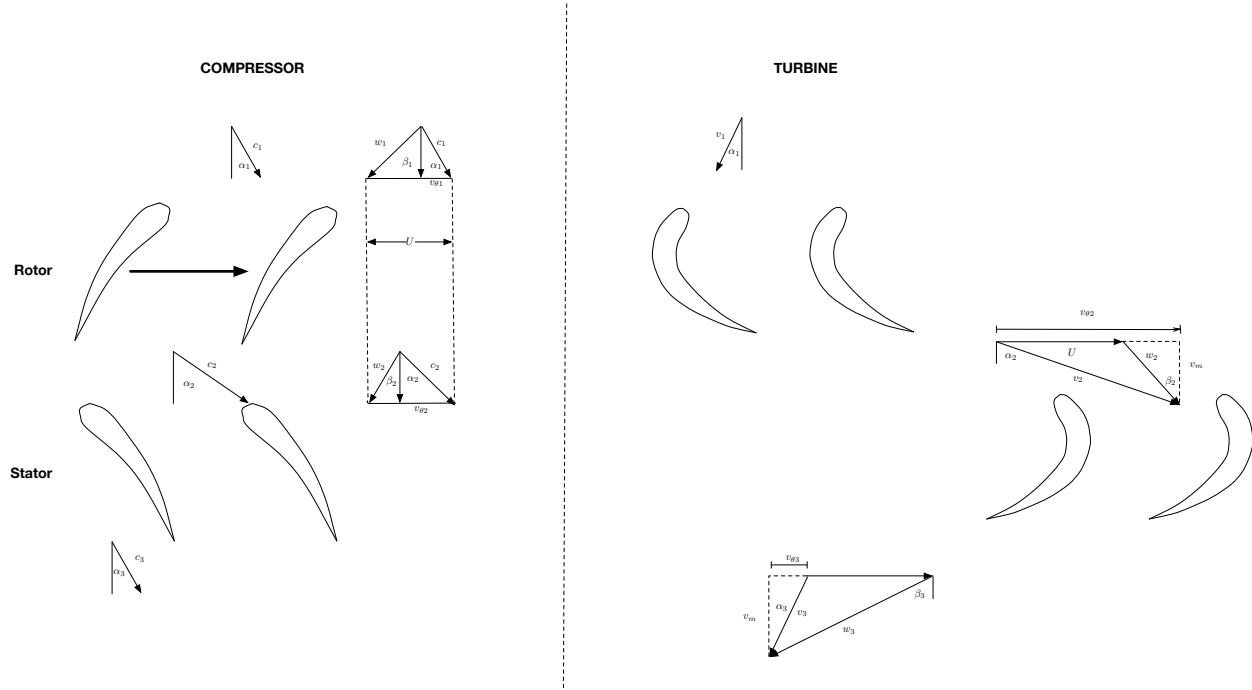
Figure 17. Blade geometry. The figure shows the angles in the fixed and rotating frames.

The Zweiffel Constant can be assumed to be 0.8 for low Mach numbers. The two are related by:

$$DF = 1 - \frac{v_2}{v_1}\left(1 - \frac{\psi_Z}{4\cos(\beta_2)}\right) \tag{28}$$

The Zweiffel Constant is estimated to be 0.8 for low Mach numbers. Pitch to chord ratios, x/c or s/l relate to Zweiffel Constant for axial turbines and Diffusion Factor for axial compressors:

$$\psi_Z = \int_0^1 (p_p - p_s)d(s/l)/(p_{t_1} - p_2) \tag{29}$$

$$DF = 1 - \frac{\cos(\alpha_1)}{\cos(\alpha_2)} + \frac{s}{l}\frac{\cos(\alpha_1)}{2}\left(\tan(\alpha_1) - \tan(\alpha_2)\right) \tag{30}$$

Repeating stages of two rows of blades are assumed so that the stage length is equal to twice the axial chord length of an individual blade.

The pressure ratio in a compressor is limited by high losses and is much lower than in a turbine. A compressor requires shaft work to increase the pressure gradient of a fluid. A turbine decreases the pressure of the fluid so that shaft work generates power. The increased pressure in the compressor means that more stages are required in the design. The stage length is controlled by the axial chord length of the blades.

American Institute of Aeronautics and Astronautics

In a turbine, the number of blades is given by the equation

$$n_{\text{blades}} = \frac{2\pi r_m}{s} \tag{31}$$

where r_m is the mean radius and s is the spacing of the blades. In the case of the turbine, the optimum space-axial chord ratio is given by

$$\frac{s}{b} = \frac{\psi_z}{\cos^2(\alpha_2)\left(\tan(\alpha_1) + \tan(\alpha_2)\right)} \tag{32}$$

If the axial chord length is found by another Zweiffel Constant relation, the spacing can be easily deduced. In the case of the compressor, the number of blades should be broken up by rotor blades and stator blades. As compressibility varies under changing pressure ratios, the pitch-to-chord ratio will also vary. For the rotor:

$$\frac{s}{l} = 2\frac{\frac{\cos(\beta_1)}{\cos(\beta_2)} - 1 - DF}{\cos(\beta_1)\left(\tan(\beta_1) - \tan(\beta_2)\right)} \tag{33}$$

For the stator:

$$\frac{s}{l} = 2\frac{\frac{\cos(\alpha_2)}{\cos(\alpha_3)} - 1 - DF}{\cos(\alpha_2)\left(\tan(\alpha_2) - \tan(\alpha_3)\right)} \tag{34}$$

If the pressure ratio exceeds the capabilities of a low-pressure axial compressor, a multi-compressor system is required. The acceptable range for a three-stage low-pressure compressor is 1.1-1.4. A high-pressure compressor consists of 10 stages and can withstand a pressure ratio as high as 23:1. The function calculates the number of compressors required and the number of stages per compressor that add to the total number of stages for the system.

Given the compressor inlet conditions and the desired conditions at the heat exchanger for Direct Fusion Drive, the engine is designed. Gas enters the compressor at 300 degrees Kelvin and 1 atmosphere. After passing through dual compressors the gas exits at 410.6 degrees Kelvin and 2 atmospheres. Turbine inlet conditions are 1589.0 degrees Kelvin and 1.9 atmospheres and turbine outlet conditions are 1263 degrees Kelvin and 1 atmosphere. The desired pressure at the heat exchanger is 1 atmosphere.

Using the design parameters for the Direct Fusion Drive model given in the diagram and the default parameters for the remaining categories, the axial compression should be performed by a two-compressor system, a low-pressure compressor of 3 stages and a high-pressure compressor of 9 stages for a total of 12 stages. There are a total of 105 blades. The overall mass of the system is 2.47 kg. The axial turbine for the Direct Fusion Drive model consists of 4 stages with a total of 61 blades and an overall mass of 6.52 kg.

IV. RF Power System

High power radio frequency heating is used in a wide variety of plasma applications. These including heating of plasmas in fusion reactors and for high power spacecraft propulsion systems such as VASIMR.[20] For tokamaks and stellarators high efficiency, while desired, is not absolutely essential since the plasmas in operational machines of this sort are expected to produce 90% of their plasma reactant heating from the plasma products. Their large size allows for absorption of the product energy. Advanced fuel reactors that employ $D-^3He$ or $p-^{11}B$ and RF heated engines need very high efficiencies in their heating systems since all of the heating is from the drive. Most RF generation systems, whether solid state or with vacuum tubes, employ linear amplifiers. These are typically Class A or B. In our design, we combined two class E amplifiers in parallel and drove the AC voltage sources 180 deg out of phase to create a push pull class E amplifier. This symmetrical design allows us to significantly reduce the degree to which even harmonics are present in the output signal. This is due to the destructive interference that results from combining the wavelength with the shifted version of itself that comes from the phase shift. We decided to utilize a gate drive between the input and the transistor. The gate drive effectively lowers the input impedance into the transistor which results in a lower charge up time so that the turn on time was much lower and the waveform much more square.

Table 6 gives the harmonics of the push-pull Class E amplifier.

An issue with Class D and E amplifiers is the EMI that is produced by the switching. Modifications to the drive can reduce EMI significantly.[21]

American Institute of Aeronautics and Astronautics
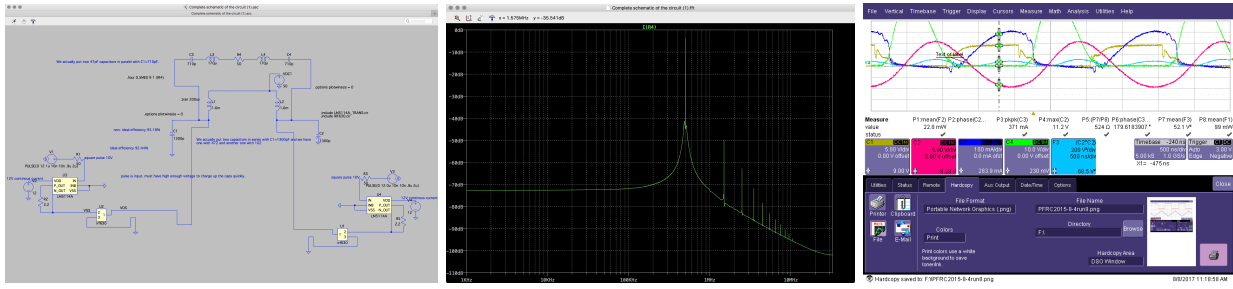
Figure 18. RF Circuit results. SPICE model, FFT and hardware test results.

Harmonic Number	Frequency (Hz)	Fourier Component	Normalized Component
1	5.000e+5	9.094e-1	1.000e+0
2	1.000e+6	2.858e-5	3.143e-5
3	1.500e+6	4.889e-3	5.376e-3
4	2.000e+6	8.002e-6	8.800e-6
5	2.500e+6	1.203e-3	1.323e-3
6	3.000e+6	4.239e-6	4.662e-6
7	3.500e+6	4.840e-4	5.322e-4
8	4.000e+6	2.685e-6	2.953e-6
9	4.500e+6	2.403e-4	2.643e-4

Table 6. The push pull shows substantial reduction in the even harmonics. Total Harmonic Distortion is 0.56%

V.   Specific Power

Table 7 gives the breakdown of the specific power for the engine. Figure 19 gives a pie chart. The resulting specific power is 0.49 kW/kg. The RF system masses and heat transfer masses are based on scaling. The RF work described in this paper points to much lower RF system mass.

Component	Value	Units
Total Engine Mass	1878.00	kg
Total Fusion Power	1.00	MW
Thrust Specific Power	0.304480	kW/kg
Engine Specific Power	0.382628	kW/kg
Fusion Specific Power	0.532318	kW/kg
Shielding Thickness	11.46	cm
Shielding	872.89	kg
Magnets	409.89	kg
Coil Cooling	17.12	kg
RMF System	109.97	kg
Power Generation	171.15	kg
Radiators	126.25	kg
Overall Structure	170.73	kg

Table 7. Specific power for the 1 MW engine.

VI.   Conclusion

This paper presents results for the power recycling subsystem of the Direct Fusion Drive. Recycled waste energy is needed to drive the fusion reactions, unlike other machines where a significant fraction of the reactant heating comes from the fusion products. Two different types of Brayton cycles, a "conventional" low-pressure Helium/Xenon cycle and a supercritical CO_2 cycle were studied. The fusion chamber heat exchanger design was presented as was the design of the RF drive. The radiator was sized. The low pressure cycle was chosen as part of the specific power roll-up. It appears that a specific power of better than 0.3

Specific power = 0.30 kW/kg

Fusion Engine Mass (1.0 MW / 1878 kg)
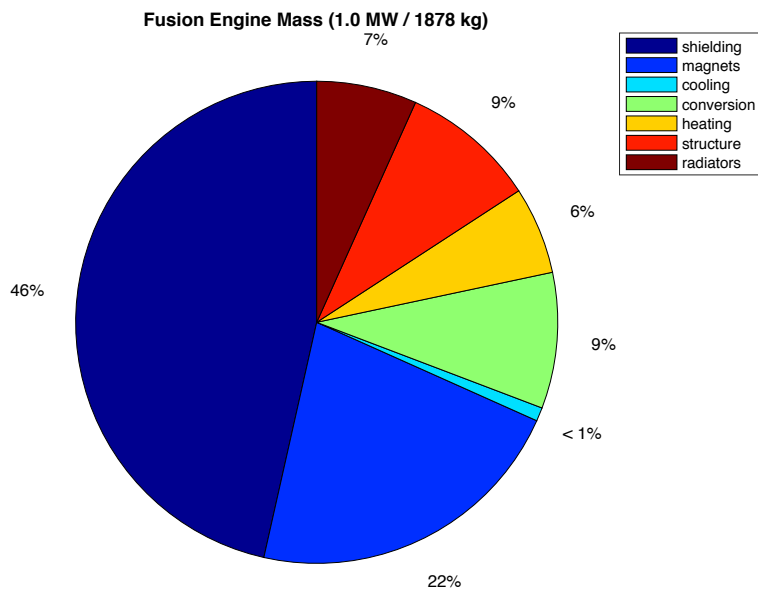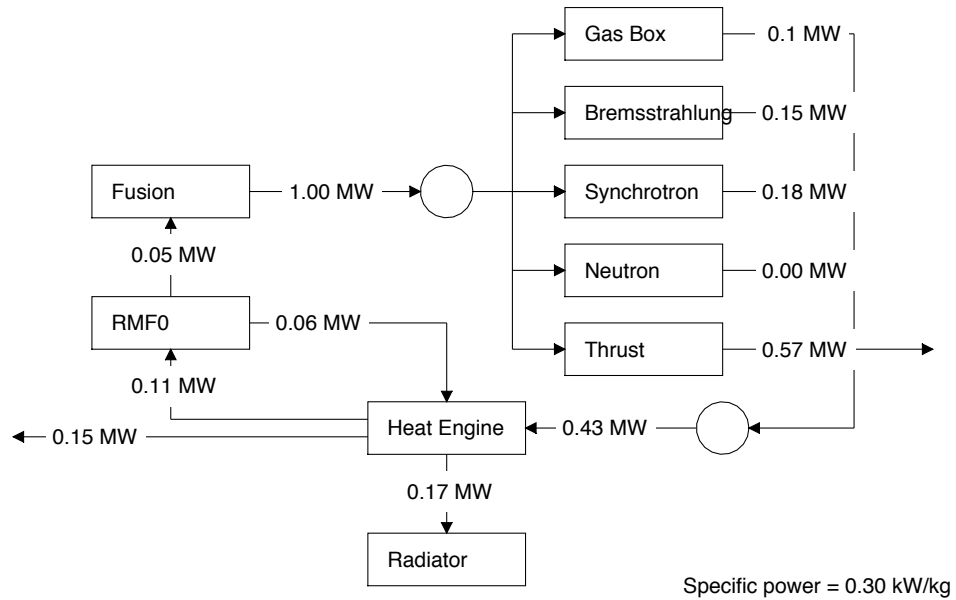
Figure 19. Power flow and mass breakdown. The radiators are a substantial portion of the mass.

American Institute of Aeronautics and Astronautics

kW/kg is achievable. The ultimate specific power is a function of a complex optimization of the subsystems described and further work is needed at the component level to arrive at the maximum specific power that can be attained for a flight system. Further work including both analysis and experiment, is needed.

VII.   Acknowledgement

References

[1] Mueller, J., Knutson, A., Paluszek, M., Pajer, G., Cohen, S. A., and Glasser, A. H., "Direct Fusion Drive for Asteroid Deflection," *33rd IEPC 2013*, October 2013, IEPC-2013-296.

[2] Paluszek, M., Pajer, G., Razin, Y., Slonaker, J., Cohen, S. A., Feder, R., Griffin, K., and Walsh, M., "Direct Fusion Drive for a Human Mars Orbital Mission," *International Astronautical Congress*, September 2014, IAC-14,C4,6.2.

[3] Cohen, S. A., Chu-Cheong, M., Feder, R., Griffin, K., Khodak, M., Klabacha, J., Meier, E., Newbury, S., Paluszek, M., Rognlien, T., Thomas, S., and Walsh, M., "Reducing Neutron Emission from Small Fusion Rocket Engines," *International Astronautical Congress*, October 2015, IAC-15,C4.7-C3.5,9,x28852.

[4] Pajer, G., Razin, Y., Paluszek, M., Glasser, A., and Cohen, S. A., "Modular Aneutronic Fusion Engine," *Space Propulsion 2012*, AAF-EAS-CNES, 2012.

[5] S. J. Thomas, M. A. Paluszek, S. A. C., "Direct Fusion Drive: Game-changing power and propulsion in space," *Proc. 20th Conference on Advanced Space Propulsion*, Glenn Research Center, November 2014.

[6] Pajer, G., Cohen, S. A., Swanson, C., Thomas, S., and Paluszek, M., "Direct Fusion Drive for Interstellar Missions," *Tennessee Valley Interstellar Workshop*, October 2017.

[7] Cohen, S. A., Swanson, C., McGreivy, N., Raja, A., Evans, E., Jandovitz, P., Khodak, M., Pajer, G., Roglien, T. D., Thomas, S., and Paluszek, M., "Direct Fusion Drive for Interstellar Exploration," *submitted to JBIS*, July 2017.

[8] Cohen, S. A., "Method To Reduce Neutron Production in Small Clean Fusion Reactors," Patent Pending, March 2012, Publication Number 20150294742.

[9] Cohen, S. A., Pajer, G., Paluszek, M. A., and Razin, Y., "Method And Apparatus To Produce High Specific Impulse and Moderate Thrust From a Fusion-Powered Rocket Engine," Patent Pending, May 2012, Publication Number 20150098543.

[10] Cohen, S. A., Stotler, D., and Buttolph, M., "Fueling Method for Small, Steady-State, Aneutronic FRC Fusion Reactors," Patent Pending, September 2013, Publication Number 20150228369.

[11] Paluszek, M., Ham, E., Cohen, S. A., and Razin, Y., "In Space Startup Method for Nuclear Fusion Rocket Engines," Patent Pending, August 2013, Publication Number 20150055740.

[12] Cohen, S. A. and Milroy, R. D., "Maintaining the closed magnetic-field-line topology of a field-reversed configuration with the addition of static transverse magnetic fields," *Physics of Plasmas*, Vol. 7, No. 6, June 2000.

[13] Cohen, S. A., Berlinger, B., Brunkhorst, C., Brooks, A., Ferarro, N., Lundberg, D., Roach, A., and Glasser, A., "Formation of Collisionless High-β Plasmas by Odd-Parity Rotating Magnetic Fields," *Physical Review Letters*, Vol. 98, 2007, pp. 145002.

[14] Evans, E. S., Cohen, S. A., and Welch, D. R., "Particle-in-cell studies of fast-ion slowing-down rates in cool tenuous magnetized plasma," *Physics of Plasmas*, Vol. 25, No. 042105, March 2018.

[15] Hubbell, J. H. and Seltzer, S. M., "X-Ray Mass Attenuation Coefficients," https://www.nist.gov/pml/x-ray-mass-attenuation-coefficients, 1996, Radiation Physics Division, PML, NIST.

[16] Bingren, S., "Core Plasma Characteristics of a Spherical Torus Fusion Reactor," *Plasma Science and Technology*, Vol. 7, No. 2, 2005.

[17] AZoM, "Silicon Carbide (SiC) Properties and Applications," 2018.

[18] Keller, C. W., Cunningham, G. R. C., and Glassford, A. P., "Final Report Thermal Performance of Multilayer Insulations," Tech. Rep. NASA CR-134477, Lockheed Missiles & Space Company, April 1974.

[19] Vliet, R. M. V., *Passive Temperature Control in the Space Environment*, MacMillan, 1965.

[20] Chang-Diaz, F., "Facts About the VASIMR Engine and its Development," 2011.

[21] Llewellyn, B., "Reduce EMI In Your Class D Amplifiers," *Electronic Design*, January 2012.

American Institute of Aeronautics and Astronautics